



Outstanding photocatalytic degradation performance under low light intensity via mitigating the quenching reaction of oxygen-centered organic radicals and oxygen

Yingyi Cheng^a, Yu-Xin Ye^{b,c,*}, Yuyan Huang^a, Huijie Yan^b, Liwei Zhang^a, Fang Zhu^{a,**}, Gangfeng Ouyang^{a,b,c}

^a Key Laboratory of Bioinorganic and Synthetic Chemistry of Ministry of Education, LIFM, School of Chemistry, IGCME, Sun Yat-sen University, Guangzhou 510275, China

^b School of Chemical Engineering and Technology, IGCME, Sun Yat-sen University, Zhuhai 519082, China

^c Southern Marine Science and Engineering Guangdong Laboratory (Zhuhai), Zhuhai, Guangdong 519082, China

ARTICLE INFO

Keywords:

Organic conjugated polymers
Oxygen-centered organic radicals
Photocatalysis
Hydrogen peroxide
Degradation

ABSTRACT

Traditional indiscriminate free radicals pose challenges to photocatalyst stability. To address this issue, oxygen-centered organic radicals (OCORs) anchored on catalyst surfaces were developed recently. However, strategies to alleviate the quenching reaction between OCORs and oxygen are lacking. Herein, the tetrasubstituted carbazole derivative-anthraquinone CZAQ-1, generating OCORs, was fabricated as photocatalyst. CZAQ-1 outperforms reported photocatalysts under low-intensity visible light, achieving 100 % degradation efficiency within 90 minutes at 10 mW·cm⁻² and 30 minutes at 100 mW·cm⁻². It exhibits exceptional stability over 10 cycles and yields hydrogen peroxide production of 3582 μmol·h⁻¹·g⁻¹ during degradation. The outstanding performance is attributed to OCORs serving as the primary oxidative active species, effectively mitigating quenching reactions with oxygen. This process is accomplished through an innovative strategy of reducing the electrostatic potential of oxygen atoms in OCORs. This study provides insights into OCORs and proposes strategies for optimizing organic polymer structures to enhance photocatalytic performance by inhibiting OCORs-oxygen reactions.

1. Introduction

The global spread of COVID-19 has led to a rapid surge in the use of pharmaceutical and disinfection products [1], including paracetamol, guaiacol, 2-chloroaniline and 4-chloroaniline, exacerbating water pollution. Such pharmaceutical and disinfection products stand out as emerging contaminants in wastewater, exerting a notably adverse impact on the ecosystem [2]. As these contaminants pose a challenge to biodegradation and traditional water treatments are unable to eliminate them [3,4], it is urgent to develop emerging technologies to degrade them. As a novel technology, without any addition of chemical reagents, photocatalysis only requires renewable light energy to activate photocatalysts to generate reactive oxygen species for the degradation of pollutants in water [5]. Based on it, photocatalysis exhibits advantages such as low cost, environmental friendliness and mild operating conditions [6,7]. Therefore, photocatalytic technology for degradation

pollutants is particularly regarded as a highly promising approach.

Organic photocatalysts have gained attention and shown great promise for practical applications in water treatment due to their tunable structure [8], optimizing photo-physical [9] and chemical processes without metal leaching [10], preventing secondary pollution [4], in comparison with inorganic photocatalysts. However, organic photocatalysts are generally connected by covalent bonds, making them susceptible to cleavage upon attack by free reactive oxygen species generated during the photocatalytic process, leading to catalyst deactivation [8,9]. This vulnerability may lead to self-decomposition and the generation of pollutants. Therefore, the stability of organic photocatalysts remains a primary challenge limiting their application in photocatalytic degradation of pollutants.

To address the aforementioned issues, it is imperative to explore new types of reactive oxygen species, reducing the formation of reactive oxygen species that could potentially attack the catalyst itself, thereby

* Corresponding author at: School of Chemical Engineering and Technology, IGCME, Sun Yat-sen University, Zhuhai 519082, China.

** Corresponding author.

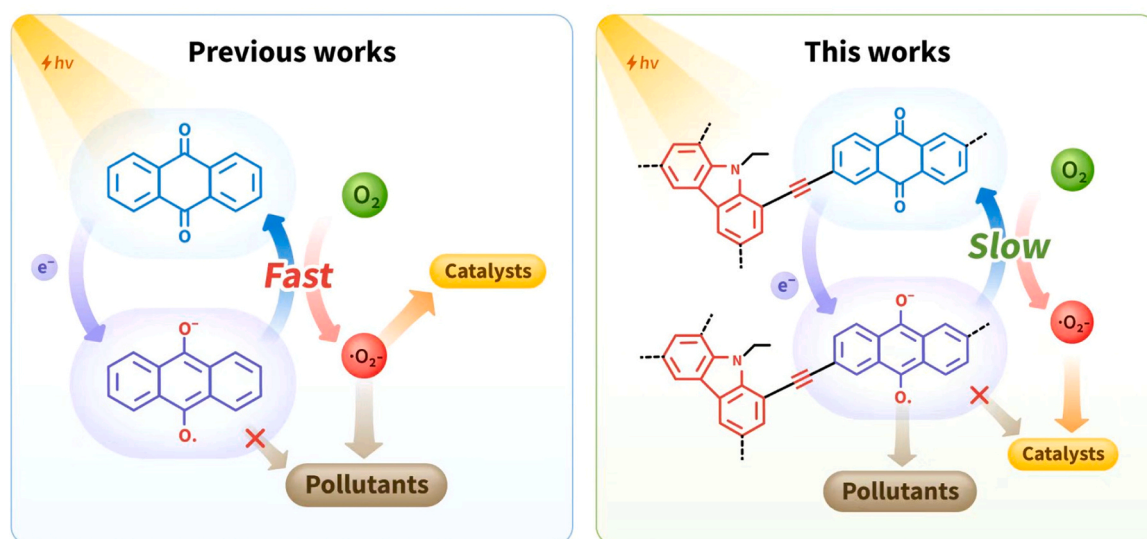
E-mail addresses: yeyuxin5@sysu.edu.cn (Y.-X. Ye), ceszhuf@mail.sysu.edu.cn (F. Zhu).

<https://doi.org/10.1016/j.apcatb.2024.124166>

Received 20 March 2024; Received in revised form 30 April 2024; Accepted 5 May 2024

Available online 8 May 2024

0926-3373/© 2024 Elsevier B.V. All rights reserved, including those for text and data mining, AI training, and similar technologies.



Scheme 1. A proposed diagram for organic conjugated polymers utilizing OCORs as major active oxygen species and slow down the quenching reaction of OCORs-oxygen in this work compared to previous work.

enhancing the stability of the photocatalytic system. In our recent research, it was found that a novel and tunable oxygen-centered organic radicals (OCORs) potentially capture electrons from organic pollutants, thereby aiding in the degradation of contaminants [11–14]. Importantly, OCORs anchored on the catalyst surface without attacking the catalyst itself. OCORs were typically formed in anthraquinone compounds, which generally featured two ketone functional groups [15]. In the process, one ketone group underwent reduction to produce a hydroxyl group, and the other ketone group maintained an unpaired electron [16]. This unpaired electron imparted strong reducing properties to OCORs, making them readily participate in free radical reactions.

In the presence of air, OCORs easily reacted with oxygen to form the stable products through a quenching reaction. The unpaired electron in OCORs was potentially donated to the oxygen molecules, giving rise to a superoxide radical [15,17]. This was facilitated by the electrophilic behavior of the double-bond structure in oxygen molecules towards free radicals. The superoxide radicals may potentially attack the organic photocatalysts, leading to catalyst deactivation. However, the strategy and regulatory mechanisms for developing novel catalysts with OCORs as the main active oxygen species to slow down the quenching reaction by oxygen have not been reported so far. Therefore, it was urgent and essential to develop novel organic conjugated polymers utilizing OCORs as reactive oxygen species and slow down the quenching reaction of OCORs by modulating the structure of organic photocatalysts, thereby enhancing its photocatalytic degradation performance, as illustrated in Scheme 1.

Herein, we synthesized a series of carbazole-acetylene-anthraquinone organic conjugated polymers (abbreviated as CzAQ-CPs) with a tetrasubstituted starburst structure and a disubstituted linear triad structure by tuning different connection sites. Among them, the tetrasubstituted starburst catalyst CzAQ-1 exhibited superior photodegradation performance for phenol. Under visible light of $100 \text{ mW} \cdot \text{cm}^{-2}$ high-light intensity, it achieved a 100 % degradation efficiency within 30 minutes, and it maintained a 100 % degradation efficiency for 90 minutes under visible light of $10 \text{ mW} \cdot \text{cm}^{-2}$ low-light intensity. CzAQ-1 also demonstrated efficient photodegradation of phenol in complicated water matrices, including tap water and lake water. Moreover, CzAQ-1 demonstrated remarkable hydrogen peroxide production under $100 \text{ mW} \cdot \text{cm}^{-2}$ visible light, reaching $3582 \mu\text{mol} \cdot \text{h}^{-1} \cdot \text{g}^{-1}$. The performance under low-intensity visible light represented the currently reported optimal results. A comprehensive

investigation of its intrinsic mechanism revealed that, tetrasubstituted catalysts CzAQ-1 exhibited a capability to decelerate the reaction between OCORs and oxygen, in comparison to the disubstituted structure. This can be ascribed to the diminished electron-donating capacity of CzAQ-1. The reduced electron-donating capacity stems from a decrease in electron cloud density, a consequence of a higher electron delocalization and an elevated number of substitutions. This study proposed valuable insights for advancing the photodegradation performance of organic photocatalysts. Significantly, for the first time it represented the comprehensive investigation of the mechanisms impeding OCORs and oxygen quenching reactions, providing a foundational understanding for future improvements.

2. Experimental section

2.1. Materials and synthesis of photocatalysts

All chemicals were purchased from commercial suppliers and used without further purification unless explicitly mentioned. The specific details of materials and the suppliers are available in [Supporting Information Section 1.1 Material](#). The detailed synthetic routes of CzAQ-CPs were outlined in [Scheme S1](#). The electronic donor and acceptor were synthesized through Sonogashira reactions via a one-pot solvothermal process to produce the photocatalyst. The specific steps of the synthesis experiment referred to [Supporting Information Section 1.6 Synthesis of Photocatalysts](#).

2.2. Characterization

Comprehensive characterization of CzAQ-CPs was conducted by different techniques, including powder X-ray diffraction (PXRD), solid nuclear magnetic resonance (^{13}C NMR), infrared spectroscopy and others. ^{13}C NMR experiments were conducted on a spectrometer (Bruker AVANCE NEO 600). PXRD patterns were carried out by X-Ray Diffractometer (D-MAX 2200VPC) at 40 kV and 26 mA with a scan rate of $10^\circ \text{ min}^{-1}$. UV-visible diffuse reflection spectroscopy (UV-Vis DRS) was performed on a Shimadzu UV-3600 spectrometer. N_2 absorption-desorption isotherms and surface area measurements were performed on a JW-BK200C instrument. SEM images were captured with a SU8010 emission scanning electron microscope operated at 10 kV. TEM images were taken using JEM-ARM200P.

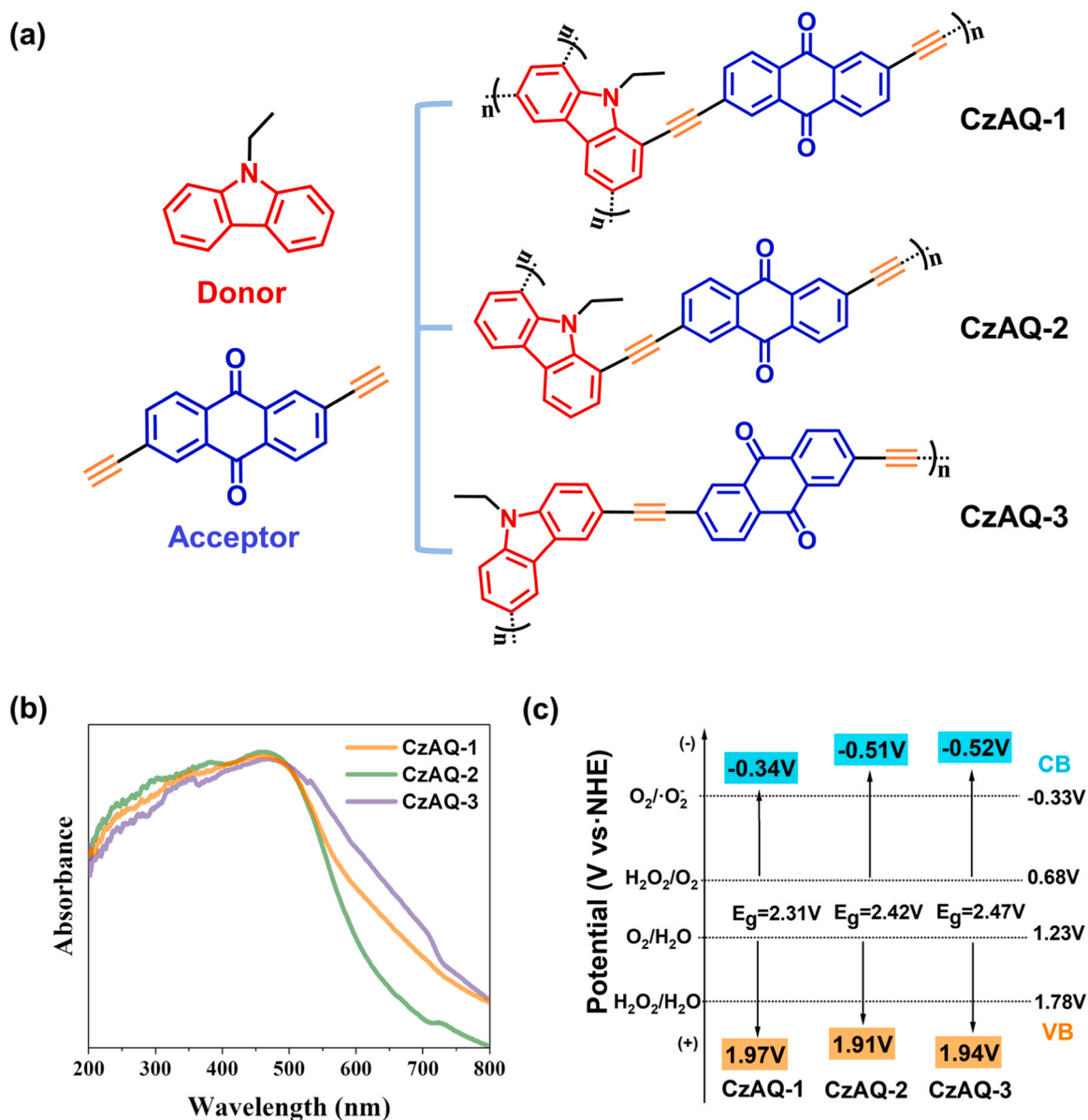


Fig. 1. (a) The molecular structures of CzaQ-CPs. (b) The UV-visible diffuse reflectance spectra of CzaQ-CPs. (c) The electronic structure.

2.3. Photocatalytic phenol degradation experiments

The catalytic performance of CzaQ-CPs was systematically investigated by photocatalytic degradation of $5 \text{ mg} \cdot \text{L}^{-1}$ phenol in deionized water under visible light condition (300 W Xe lamp with a 400 nm cut-off filter) at room temperature. The average light intensity was kept at $100 \text{ mW} \cdot \text{cm}^{-2}$ or $10 \text{ mW} \cdot \text{cm}^{-2}$. In the experimental setup, 5 mg photocatalyst was dispersed in 50 mL deionized water with $5 \text{ mg} \cdot \text{L}^{-1}$ phenol. To establish adsorption-desorption equilibrium between the substances and the catalysts, all photodegradation solutions were stirred in the dark for 30 minutes. Subsequently, the solutions were irradiated by the Xe lamp and sampled at 10 minutes intervals for 1 hour. At predetermined time points, approximately 0.7 mL of suspension was sampled and filtrated through a $0.22 \mu\text{m}$ membrane filter to remove photocatalyst particles. The residual concentration of phenol in suspension was quantified by high-performance liquid chromatography (Shimadzu LCMS-2020) equipped with a C18 column ($4.6 \times 250 \text{ mm}$, $5 \mu\text{m}$, Agilent).

3. Result and discussion

3.1. Catalysts synthesis and the chemical structures

As carbazole typically exhibited the characteristics of donating electrons and the electron-deficient nature of anthraquinone, these two monomers were employed as electron donor and electron acceptor to form the photocatalysts by polymerization process, respectively. The electron donor- π -acceptor (D- π -A) conjugated polymer was synthesized with 1,3,6,8-tetrabromo-9-ethyl-carbazole as an electron-donor, 2,6-diethynyl-9,10-anthracenedione (AQ) as an electron acceptor with alkynyl as a connector, named CzaQ-1 (Fig. 1a). To investigate the impact of different substitution positions and quantities on photocatalytic performance, two comparative photocatalysts with different electron donor were synthesized. For comparison, analogous D- π -A conjugated polymers of CzaQ-2 with 1,8-dibromo-9-ethyl-carbazole and CzaQ-3 with 3,6-dibromo-9-ethyl-carbazole as an electron donor were also synthesized (Fig. 1a), respectively.

The chemical structure of CzaQ-CPs was thoroughly characterized through experiments such as Fourier transform infrared spectra (FT-IR),

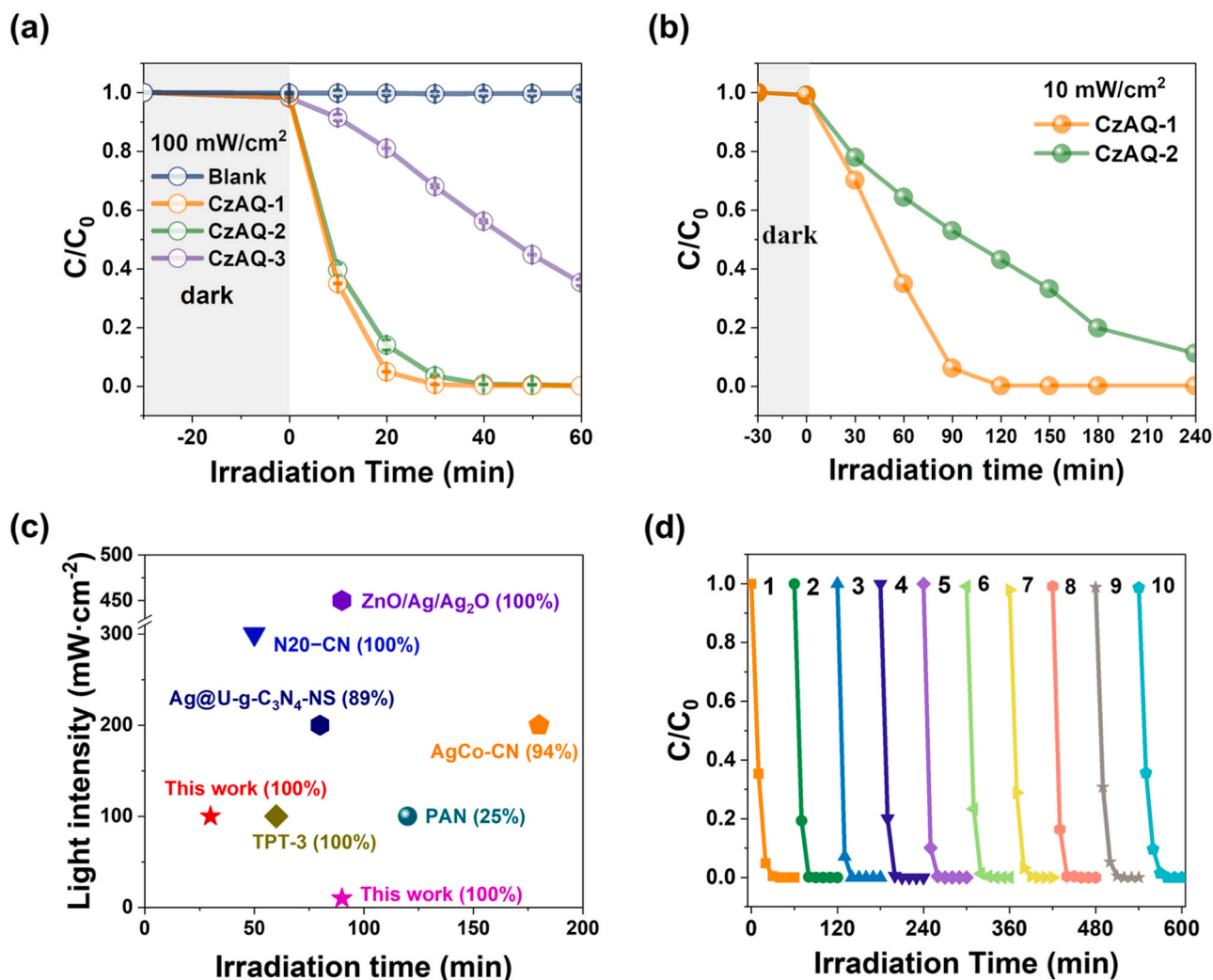


Fig. 2. Phenol degradation time profiles of CzaQ-CPs under visible light of (a) 100 mW/cm² and (b) 10 mW/cm². (c) The comparison of phenol photocatalytic degradation efficiency of CzaQ-1 with other reported photocatalysts. (d) Recyclability in phenol degradation of CzaQ-1.

solid nuclear magnetic resonance (NMR), powder X-ray diffraction (PXRD) and other analyses. In FI-IR (Fig. S5a), the terminal $\equiv\text{C-H}$ stretching vibration at 3257 cm^{-1} of 2,6-diethynyl-9,10-anthracenedione vanished upon polymerization, accompanied by the increase of the $\text{C}\equiv\text{C}$ vibration at 2200 cm^{-1} , indicating that the two monomers were effectively joined through the alkyne group [18]. It was further confirmed by the solid-state ^{13}C NMR (Fig. S5b-d) as the characteristic peaks of the alkyne carbons displayed at $\approx 90\text{--}110\text{ ppm}$ ($\text{C}\equiv\text{C}$) [19]. After the polymerization, both the carbonyl groups and ethyl groups connected to nitrogen atoms were still retained. The characteristic peaks of $\text{C}=\text{O}$ vibrations at 1669 cm^{-1} in IR, and keto carbons at $\approx 180\text{ ppm}$ ($\text{C}=\text{O}$), alkyl carbons at $\approx 20\text{--}40\text{ ppm}$ ($\text{N-CH}_2\text{CH}_3$) and aromatic carbons at $\approx 120\text{--}140\text{ ppm}$ ($\text{C}=\text{C}$) in the solid-state ^{13}C NMR were also proved the successful polymerization for all catalysts [12,20]. The broad peaks observed at $10\text{--}30$ degrees in PXRD (Fig. S6) indicated an amorphous carbons feature for the photocatalysts [21]. The scanning electron microscopy (SEM) images and transmission Electron Microscope (TEM) images (Fig. S7-S8), both analyses indicated that all CzaQ-CPs exhibited laminar stacking structures attributed to robust $\pi\text{-}\pi$ interactions [22]. According to the Brunauer-Emmett-Teller (BET) surface area measurement (Fig. S9 and Table S1), the specific surface area was $155.4\text{ m}^2\cdot\text{g}^{-1}$, $65.1\text{ m}^2\cdot\text{g}^{-1}$ and $49.4\text{ m}^2\cdot\text{g}^{-1}$ for CzaQ-1, CzaQ-2 and CzaQ-3, respectively. In comparison to CzaQ-2 and CzaQ-3, the increased BET surface area of CzaQ-1 potentially contributed to the enhancement of

photocatalytic performance [23].

3.2. The electronic structures

The UV-vis DRS spectra (Fig. 1b) showed that all CzaQ-CPs exhibited a broad absorption band in the visible range of $400\text{--}700\text{ nm}$. As visible light constitutes approximately 47 % of the total solar radiation energy, the broad absorption band of visible light of CzaQ-CPs facilitated efficient utilization of solar energy. The conduction band potential of CzaQ-CPs was calculated from the Flat-band potential via Mott-Schottky tests (Fig. S10). And the valence band potential of CzaQ-1, CzaQ-2 and CzaQ-3 were determined to be 1.97 V, 1.91 V and 1.94 V versus the Normal Hydrogen Electrode (NHE) based on valence bands X-ray photoelectron spectroscopy tests and the Scanning Kelvin Probe Force Microscopy (Fig. S11-S12). The detail calculation was available on Supporting Information Section 2.1. Thus, the electronic band structures of CzaQ-CPs were displayed in Fig. 1c, indicating that all catalysts possessed sufficiently high reduction potentials to generate $\cdot\text{O}_2^-$ ($\text{O}_2/\cdot\text{O}_2^-$, -0.33 V) [24]. Apparently, the appropriate oxidation/reduction potentials for CzaQ-CPs underscored their significant potential for the photocatalytic degradation of aqueous organic pollutants.

To elucidate the electronic donor and acceptor properties of three fabricated organic conjugated polymers, Density Functional Theory (DFT) calculations were performed at B3LYP/6-31 G** level with

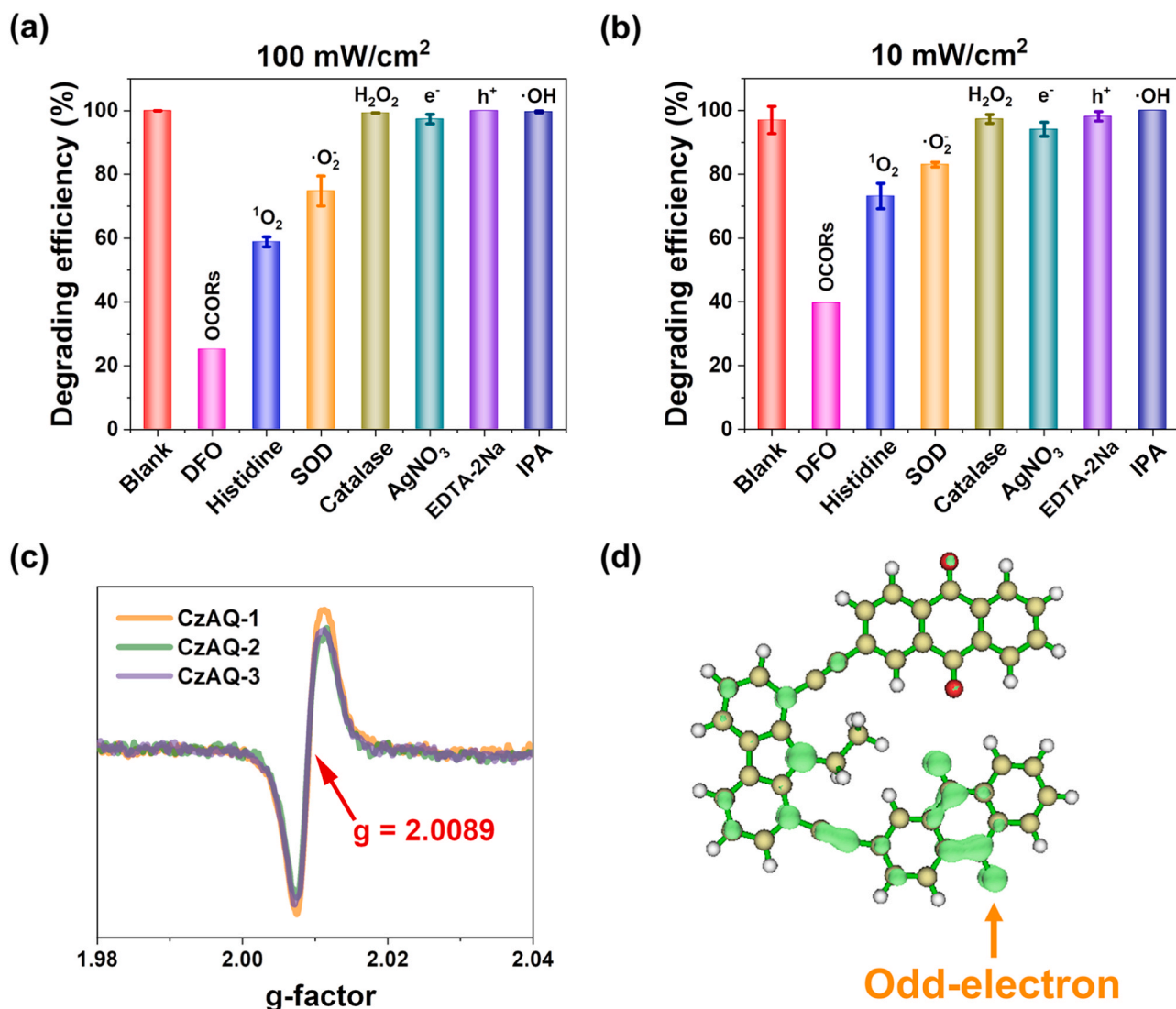


Fig. 3. Phenol degradation efficiency with different sacrificial agents under visible light of (a) 100 mW/cm² and (b) 10 mW/cm². (c) The EPR spectra of CzaQ-CPs in the dark. (d) The odd-electron density in a single CzaQ-2 unit through TD-DFT.

simplified fragments [25]. As showed in Fig. S13, the highest occupied molecular orbitals (HOMOs) were situated on the carbazole-based units and the lowest unoccupied molecular orbitals (LUMOs) were predominantly located on the anthraquinone moiety. As the electron-donating capability of the N atom can be extensively delocalized throughout the entire donor structure, the separate HOMOs were primarily situated on the entirety of the carbazole units [26]. Therefore, appropriate Donor-Acceptor (D-A) pairs were confirmed in CzaQ-CPs, with the carbazole moiety exhibiting electron-donating capability and the anthraquinone moiety demonstrating excellent electron-accepting capability.

3.3. Photocatalytic degradation performance for organic pollutant

The photocatalytic performance of the CzaQ-CPs was evaluated by examining their degradation efficiency using phenol as a representative example. To investigate the potential adsorption of phenol by the catalysts, the mixture of catalysts and phenol was stirred in the dark for 4 hours. As depicted in Fig. S14a, the observed adsorption amount was found to be negligible. Consequently, the adsorption equilibrium time for phenol was determined to be 30 minutes. Phenol exhibited no inherent self-degradation and showed minimal degradation without

photocatalysts under visible light (Fig. 2a). Initially, the catalyst dosage was optimized. There was no significant increase in performance beyond a dosage of 5 mg (Fig. S14b). Consequently, 5 mg was determined as the optimal dosage.

The photocatalytic experiment was conducted under simulated sunlight irradiation ($\lambda > 400$ nm) in deionized water with open air. No supplementary organic reagents were introduced into the reaction vials. When the intensity of visible light irradiation was set at 100 mW·cm⁻², CzaQ-1 and CzaQ-2 achieved complete degradation of phenol within 30 and 40 minutes, respectively, while CzaQ-3 only degraded 65 % of phenol in 1 hour (Fig. 2a). It was noteworthy that under such 100 mW·cm⁻² high-intensity visible light, CzaQ-1 and CzaQ-2 exhibited similar degradation performance. However, under identical conditions except the light intensity decreasing from 100 mW·cm⁻² to 10 mW·cm⁻², the degradation performance of CzaQ-1 significantly surpassed that of CzaQ-2. CzaQ-1 achieved 100 % degradation of phenol in 90 minutes, whereas CzaQ-2 only degraded 89 % of phenol even with the extended time of 240 minutes (Fig. 2b). CzaQ-1 degraded phenol completely within 60 minutes even though the concentration of phenol increases from 5 mg·L⁻¹ to 20 mg·L⁻¹ (Fig. S14c). Moreover, CzaQ-1 degraded phenol completely within 3 hours even though the light intensity was reduced to 2 mW·cm⁻² (Fig. S14d). Notably, CzaQ-1

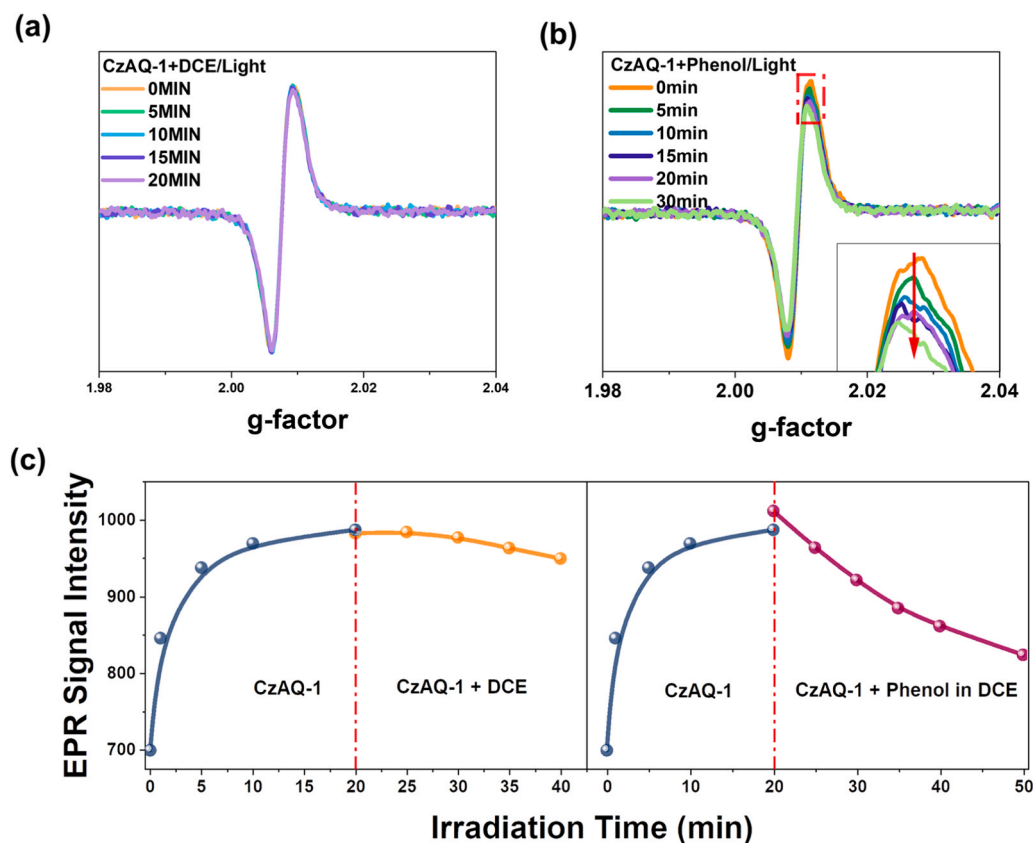


Fig. 4. The EPR spectra of CzaQ-1 with (a) DCE and (b) solution of phenol in DCE under irradiation with time. (c) The comparison of EPR signal intensities of (a) and (b).

demonstrated superior photocatalytic degradation performance towards phenol both under high and low-intensity visible light, surpassing that of recently reported photocatalysts in deionized water under similar conditions (Fig. 2c and Table S3). Furthermore, CzaQ-1 exhibited remarkable hydrogen peroxide production of $3582 \mu\text{mol}\cdot\text{h}^{-1}\cdot\text{g}^{-1}$ even during the phenol degradation process, outperforming the reported H_2O_2 photosynthetic systems (Fig. S14e-f).

In addition, the recyclability of CzaQ-1 was assessed through ten reused cycles of phenol degradation. Similar to the first time, the reused catalysts also remained outstanding photocatalytic degradation performance of phenol, which suggesting that the degradation efficiency of CzaQ-1 could be maintained for at least ten cycles (Fig. 2d). The FT-IR spectra, XRD and SEM images of CzaQ-1 were recorded after reused, and no significant changes were observed (Fig. S15). Evidently, CzaQ-1 demonstrated excellent recyclability and stability, making it suitable for repeated use in the degradation of phenol.

3.4. The identification of reactive oxygen species

CzaQ-1 and CzaQ-2 exhibited similar photocatalytic degradation performance under high-intensity visible light, but notable distinctions arose under low-intensity irradiation conditions. To discern potential differences in the active species of CzaQ-1 under various intensities of visible light, a comprehensive investigation of the associated reactive oxygen species (ROS) was conducted through free radical quenching experiments. Various scavengers, including deferoxamine (DFO) [27], L-histidine, Superoxide dismutase (SOD), catalase, silver nitrate (AgNO_3), ethylenediaminetetraacetic acid disodium salt ($\text{EDTA}\cdot 2\text{Na}$) and isopropyl alcohol (IPA) were employed to quench OCOR, singlet oxygen ($^1\text{O}_2$), superoxide radicals ($\cdot\text{O}_2^-$), hydrogen peroxide (H_2O_2), electron (e^-), hole (h^+) and hydroxyl radicals ($\cdot\text{OH}$), respectively [22, 28]. The degradation towards phenol faced significantly inhibition in

the presence of DFO, L-histidine and SOD under both high-intensity ($100 \text{ mW}\cdot\text{cm}^{-2}$) and low-intensity ($10 \text{ mW}\cdot\text{cm}^{-2}$) visible light. This observation suggested that OCORs predominantly served as the principal ROS under different light intensities, while $^1\text{O}_2$ and $\cdot\text{O}_2^-$ played minor roles in the photocatalytic degradation of phenol, as illustrated in Figs. 3a and 3b. Nevertheless, the inhibitory effects of the three active species differed under different irradiation conditions. Under high-intensity visible light, DFO inhibited the degradation efficiency of phenol by 75 %, histidine inhibited by 41 % and SOD inhibited by 25 %. In condition of low-intensity visible light, DFO impeded the degradation efficiency by 60 %, histidine impeded by 27 %, and SOD impeded by 17 %. This emphasized the crucial role of OCORs in the process of phenol degradation, especially under conditions of low-intensity visible light.

To substantiate the presence of OCORs, the single electron signals of solid materials can be determined through Electron Paramagnetic Resonance (EPR) testing. The EPR spectrum under argon of CzaQ-1 existed one hyperfine splitting signal ($g = 2.0089$) [13,29,30], which was assigned to the OCORs on CzaQ-1 (Fig. 3c). DFT calculations further identified the distribution sites of single electrons, providing evidence that the excited odd electron was located in the O atom of the AQ group (Fig. 3d and Fig. S16).

To further demonstrate the involvement of OCORs in phenol degradation, the concentration of OCORs was monitored by in-situ EPR [31,32]. The in-situ EPR testing method proceeded as follows: A specific quantity of solid catalysts was loaded into a capillary and exposed it to light for a certain duration. Subsequently, a high-concentration solution of phenol, dissolved in 1,2-dichloroethane, was introduced, and the material solution continued to be irradiated. EPR signals were recorded at regular intervals. A control trial was established by introducing an equivalent amount of 1,2-dichloroethane solvent. It was noteworthy that the EPR signal of OCORs in the solid catalyst significantly increased

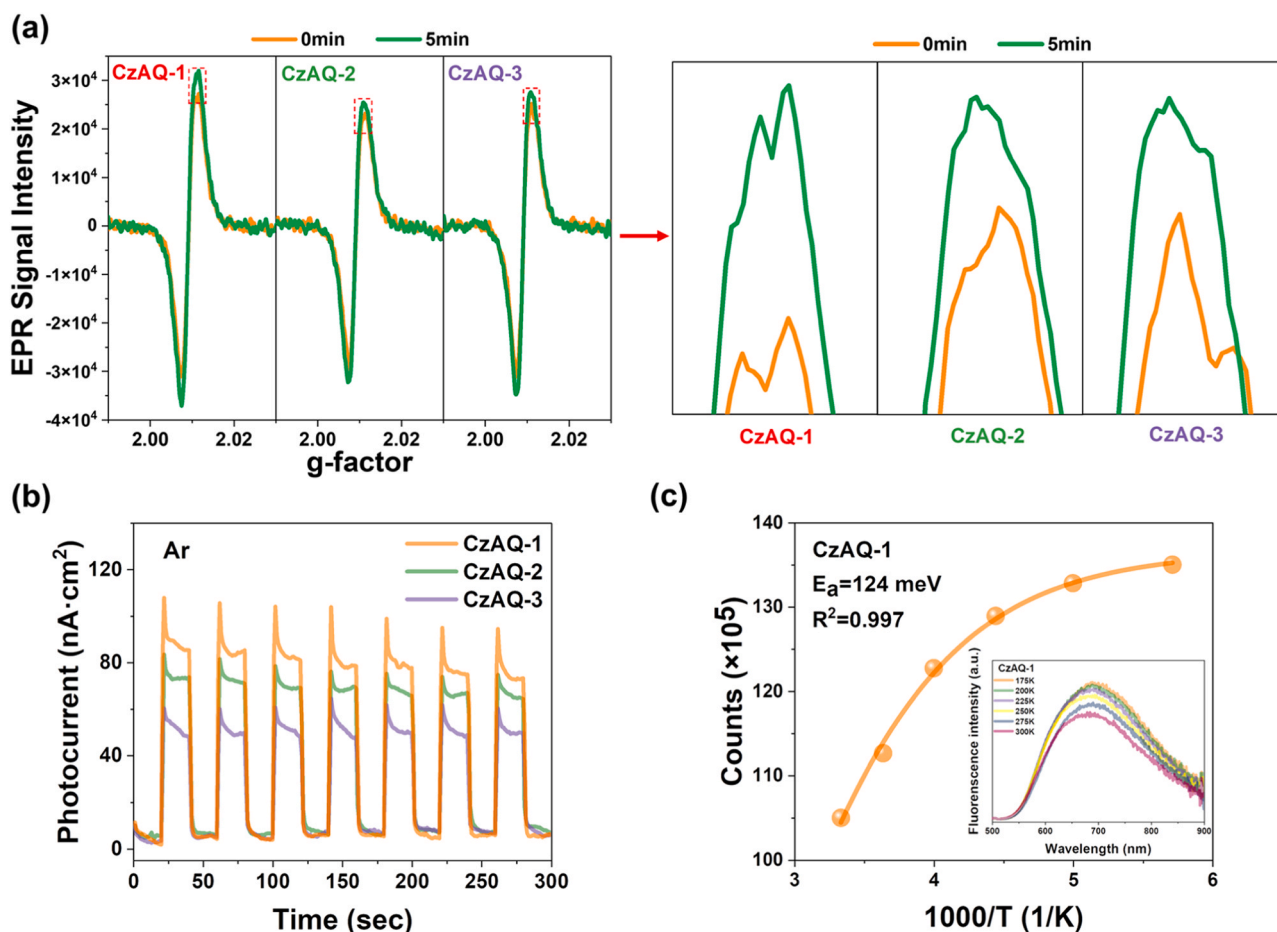


Fig. 5. (a) The signal intensity increments of OCORs for CzAQ-CPs after a 5-minute irradiation and its enlarged drawing. (b) The transient photocurrent responses of CzAQ-CPs. (c) Temperature-dependent photoluminescence spectra for CzAQ-1.

over time under light irradiation (Fig. S17). Upon the addition of phenol, the concentration of OCORs decreases significantly over time (Fig. 4b). In contrast, the control trial with added solvent showed minimal change in OCORs signal (Fig. 4a). As shown in Fig. 4c, this observation clearly demonstrated that OCORs generated by CzAQ-1 under illumination can react with phenol, providing further evidence for the pivotal role of OCORs in the degradation process.

3.5. Intrinsic mechanisms influencing OCORs concentration

Fig. 5a depicted the signal intensity increment of OCORs for CzAQ-CPs after a 5-minute exposure to light. Notably, CzAQ-1 demonstrated the most significant increment, whereas CzAQ-2 and CzAQ-3 exhibited relatively lower increases. A comprehensive investigation was conducted on the intrinsic mechanisms influencing the generation concentration of OCORs. The generation process of OCORs was detailed in our previous publication [11–13]. Under the photoexcitation of photocatalysts, excitons were generated and then separated, leading to the generation of photoinduced charge carriers. Subsequently, photoexcited electrons from donor migrated intramolecularly to AQ moiety and reduced the C=O double bond in AQ into a C-O· radical. Thus, the efficiency of exciton dissociation and electron transfer from donor to acceptor within the catalysts had a potentially significant impact on the formation of OCORs.

To reveal the efficiency of exciton dissociation, photocurrent measurements were conducted (Fig. 5b), revealing that CzAQ-1 efficiently generated a greater number of photogenerated electron-hole than CzAQ-2 and CzAQ-3. The fluorescence spectroscopy quantum yields of CzAQ-

CPs were all below detection level. In order to unveil the remarkably low fluorescence quantum yields of CzAQ-CPs, temperature-dependent photoluminescence (PL) spectra were used to characterize the radiative recombination of excitons. A thermal quenching phenomenon of PL emission in the temperature range from 175 to 300 K was observed for the CzAQ-CPs (Fig. 5c and Fig. S18). The integrated PL intensities as a function of temperature was fitting by the Arrhenius equation as following.

$$I(T) = I_0 / (1 + A e^{-\frac{E_a}{k_B T}})$$

The exciton activation energy (E_a) of the PL quenching process was estimated to be 124, 147 and 174 meV for CzAQ-1, CzAQ-2 and CzAQ-3 respectively. This demonstrated that CzAQ-1 efficiently promoted its exciton dissociation due to its lower E_a [33]. Therefore, CzAQ-1 showcased the highest formation of photogenerated carriers, underscoring its superior efficiency in exciton dissociation.

Furthermore, it is crucial to explore the ultrafast charge transfer by femtosecond transient absorption (TA) spectroscopy. The rapid decrease in the amplitude of excited state absorption (ESA) signal in the presence of AgNO₃ as electron scavengers, contrasted with their slight increase in the presence of triethylamine (TEA) as hole scavengers (Fig. 6a-c and Fig. S19), led to the assignment of ESA signals between 600 and 750 nm to photoinduced electrons [34]. The lifetime of these photoinduced electrons was attributed to intramolecular electron transfer from the electron donor to the acceptor [35]. Given the similar electron donor and acceptor characteristics of CzAQ-CPs, their photoinduced electron lifetimes were very close (Fig. 6d) and followed an increasing order: CzAQ-1 (920 ps) < CzAQ-2 (1082 ps) < CzAQ-3 (1098 ps).

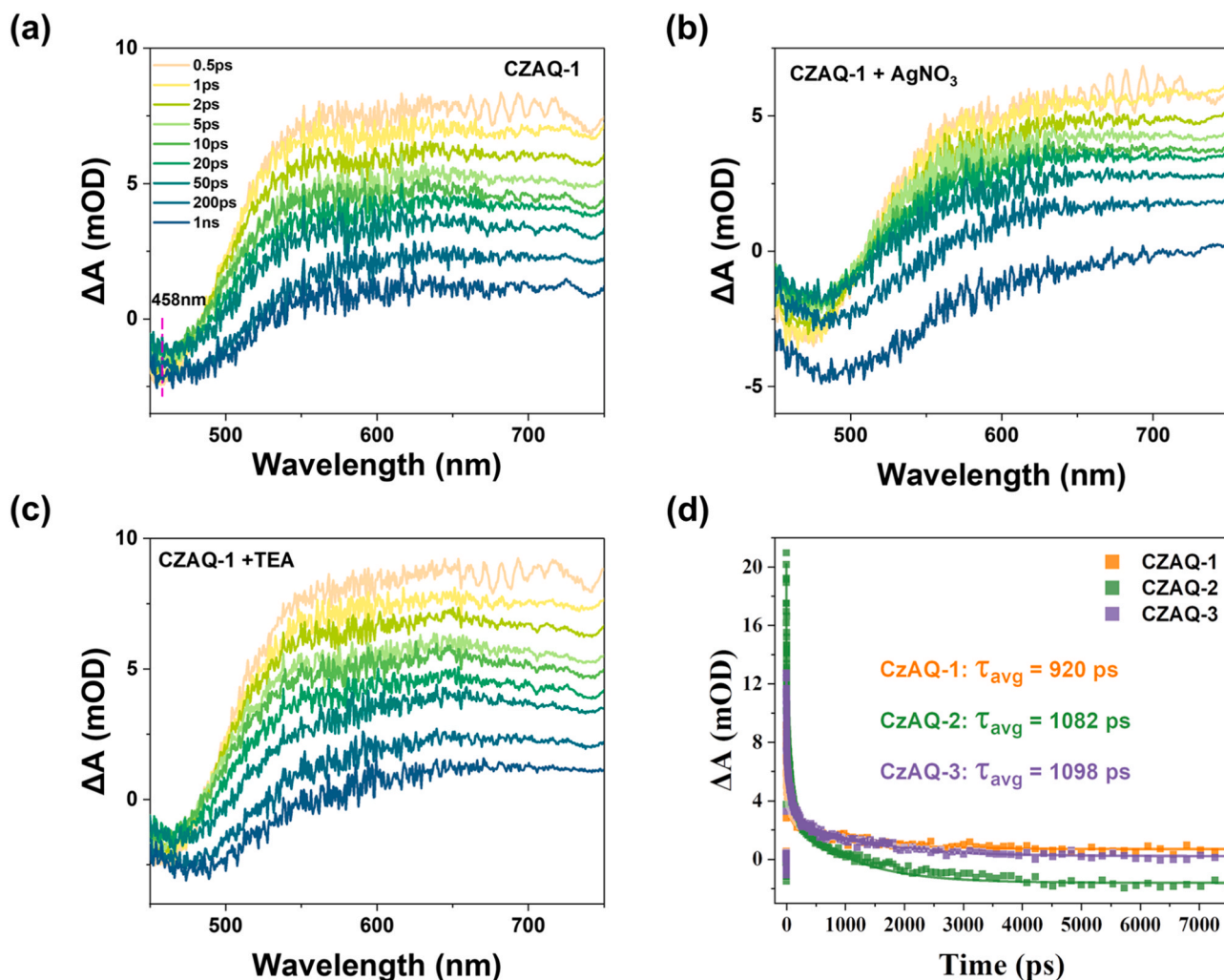


Fig. 6. TA spectra of CzaQ-1 (a) blank, (b) with AgNO₃ (10 mM) and (c) with triethylamine (TEA, 10 mM). (d) Comparison of TA kinetic traces of CzaQ-CPs.

In order to further explore the factors influencing the electron transfer efficiency, hole-electron analysis in the first excited-state were utilized to elucidate the process of electron transfer. The hole–electron distribution diagrams of CzaQ-CPs, illustrated in the Fig. S20, revealed that excited electrons transferred from the carbazole moiety to AQ units through intramolecular charge transfer (IRCT) process [36]. Nevertheless, substantial differences existed in electron transfer during IRCT process among CzaQ-CPs. The distinction can be further elucidated by two parameters *Sr* index and *D_{CT}* index, where *Sr* index represented the calculated overlap integral of hole-electron distribution and the *D_{CT}* index represented the calculated distance between the hole and electron centroids. A smaller *Sr* index and a larger *D_{CT}* index indicated a more effective electron transfer. CzaQ-1 showed the smallest *Sr* index (0.36657 a.u.) and the largest *D_{CT}* (7.220 Å), indicating the highest electron transfer efficiency in IRCT (Fig. S20 and Table S2) [36, 37]. The above results all suggested that CzaQ-1 exhibited superior properties in both exciton dissociation and electron transfer compared to CzaQ-2 and CzaQ-3, which constituted the critical factors influencing the concentration of OCORs.

3.6. OCORs quenching

As OCORs had an unpaired electron, it was susceptible to quenching by oxygen in the surrounding environment to generate superoxide radicals [38]. All three catalysts exhibited EPR signals (*g*=2.0089) of OCORs. To further explore the differences in OCORs reactions with

oxygen in various chemical environments, the photoexcited states of OCORs in CzaQ-CPs under argon and oxygen conditions were comprehensively investigated through in-situ solid-state EPR experiments. The OCORs signal in CzaQ-1 increased upon exposure to light and spontaneously decreased upon light cessation under argon atmosphere (Fig. 7a-b), indicating that the formation of OCORs was light-responsive [31]. Following the cessation of light exposure, the OCORs signals in CzaQ-1 exhibited a gradual decline, reverting to the pre-illumination level after 15 minutes (Fig. 7c-d). This signified a sustained duration of approximately 15 minutes for OCORs, demonstrating the stability of OCORs. When the atmosphere changed from argon to oxygen, the variation trend of OCORs in CzaQ-1 remained consistent (Fig. 8a). The EPR signal intensity increased upon illumination, signifying a relatively sluggish reaction with oxygen. Similar to the phenomenon observed with CzaQ-1, the signals of OCORs in CzaQ-2 increased over time under argon atmosphere during illumination (Fig. S21a). However, a complete reversal of the in-situ EPR phenomena occurred when the atmosphere conditions changed from Ar to O₂. Under oxygen atmosphere with visible light irradiation, the OCORs signal in CzaQ-2 gradually decreased over time (Fig. 8b). This evidence (Fig. 8c) illustrated that OCORs in CzaQ-2 reacted with oxygen more rapidly than that in CzaQ-1. Moreover, the OCORs reacted with oxygen to generate ·O₂⁻, which could be confirmed by the EPR experiment as the spin trap 5, 5-Dimethyl-1-Pyrroline-N-oxide (DMPO) captured a weak signal of ·O₂⁻ in the dark (Fig. S21b).

To verify the enhanced stability of OCORs in tetrasubstituted CzaQ-

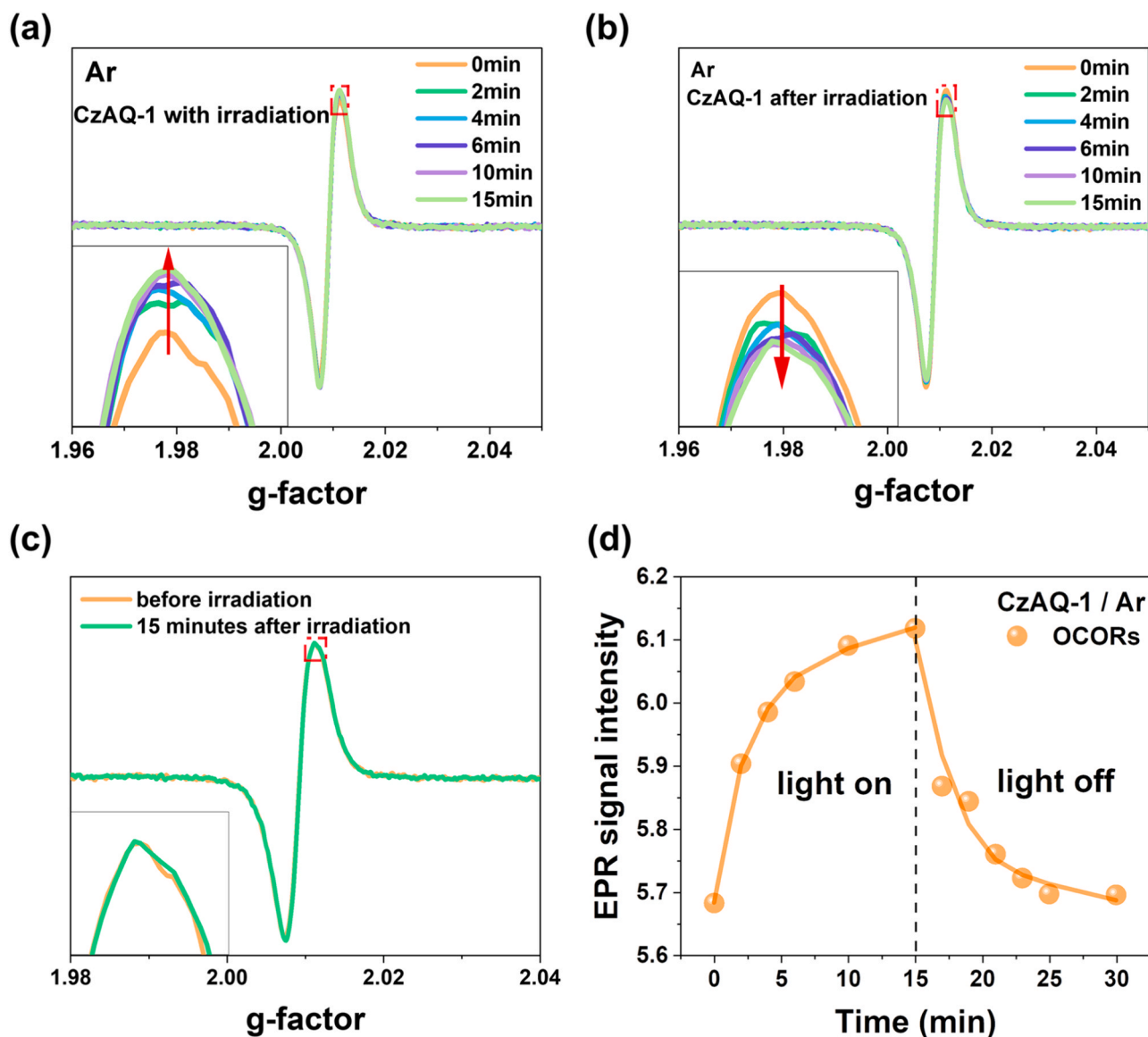
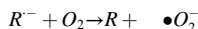


Fig. 7. The EPR spectra of CzAQ-1 for (a) under light irradiation, (b) after turning off light and (c) comparison in dark and after turning off light for 15 minutes under Ar atmosphere. (d) The EPR signal intensities change with time of CzAQ-1.

1, cyclic voltammetry (CV) experiments were performed. As shown in the Fig. S22, CzAQ-CPs all exhibited a one electron reduction process of anthraquinone[39]. The oxidation potentials for CzAQ-1, CzAQ-2, and CzAQ-3 were 1.15 V, 1.06 V, and 1.09 V versus Ag/AgCl, respectively. In comparison to CzAQ-2, the larger anodic shift (90 mV) observed in CzAQ-1 provided direct evidence for the enhancement of the thermodynamic stabilization of OCORs. In order to clarify the disparities in the reactivity between OCORs in CzAQ-CPs and oxygen (as per the follow equation), the Gibbs Free Energy (ΔG) of the reaction was computed by Gaussian software.



where R represented OCORs in CzAQ-1 and CzAQ-2. The calculated ΔG for the reactions with CzAQ-1 and CzAQ-2 were 1.96 eV and 1.08 eV, respectively (Fig. 8d). CzAQ-1 displayed a higher ΔG for the reaction between OCORs and oxygen, indicating that OCORs in CzAQ-1 encountered greater difficulty in reacting with oxygen. This provided additional confirmation that CzAQ-2 reacts with oxygen more readily than CzAQ-1. In order to elucidate the factors contributing to the higher ΔG , an investigation was initiated to explore variations in electron-

donating abilities of OCORs in CzAQ-1 and CzAQ-2 and to delve into the electron cloud density of the electron acceptor. The atomic dipole corrected Hirshfeld atomic charge (ADCH) distribution rendered with VMD software highlighted that all oxygen atoms in both CzAQ-1 and CzAQ-2 exhibited negative charges (Fig. S23a-b) [40,41]. Furthermore, the charge distribution among these atoms was found to be remarkably consistent. Electrostatic potential maps were undertaken to further explore the charge distribution of CzAQ-1 and CzAQ-2 and the reactivity of oxygen atoms. As shown in Fig. S23c-d, the electrostatic potential of the oxygen atoms in CzAQ-2 tended to be more negative compared to CzAQ-1. This implied a higher probability of electron donation for OCORs in CzAQ-2, rendering it more susceptible to quenching reactions with oxygen [42].

In conclusion, under $100 \text{ mW} \cdot \text{cm}^{-2}$ high-intensity visible light, owning a high optical quantum density, the rapid formation of OCORs by CzAQ-2 minimized the impact of oxygen quenching on the OCORs intensity. Furthermore, the extended lifetimes of OCORs enabled effective waiting for pollutant diffusion without compromising degradation performance. Consequently, the degradation performances of CzAQ-1 and CzAQ-2 were similar under high-intensity visible light. However,

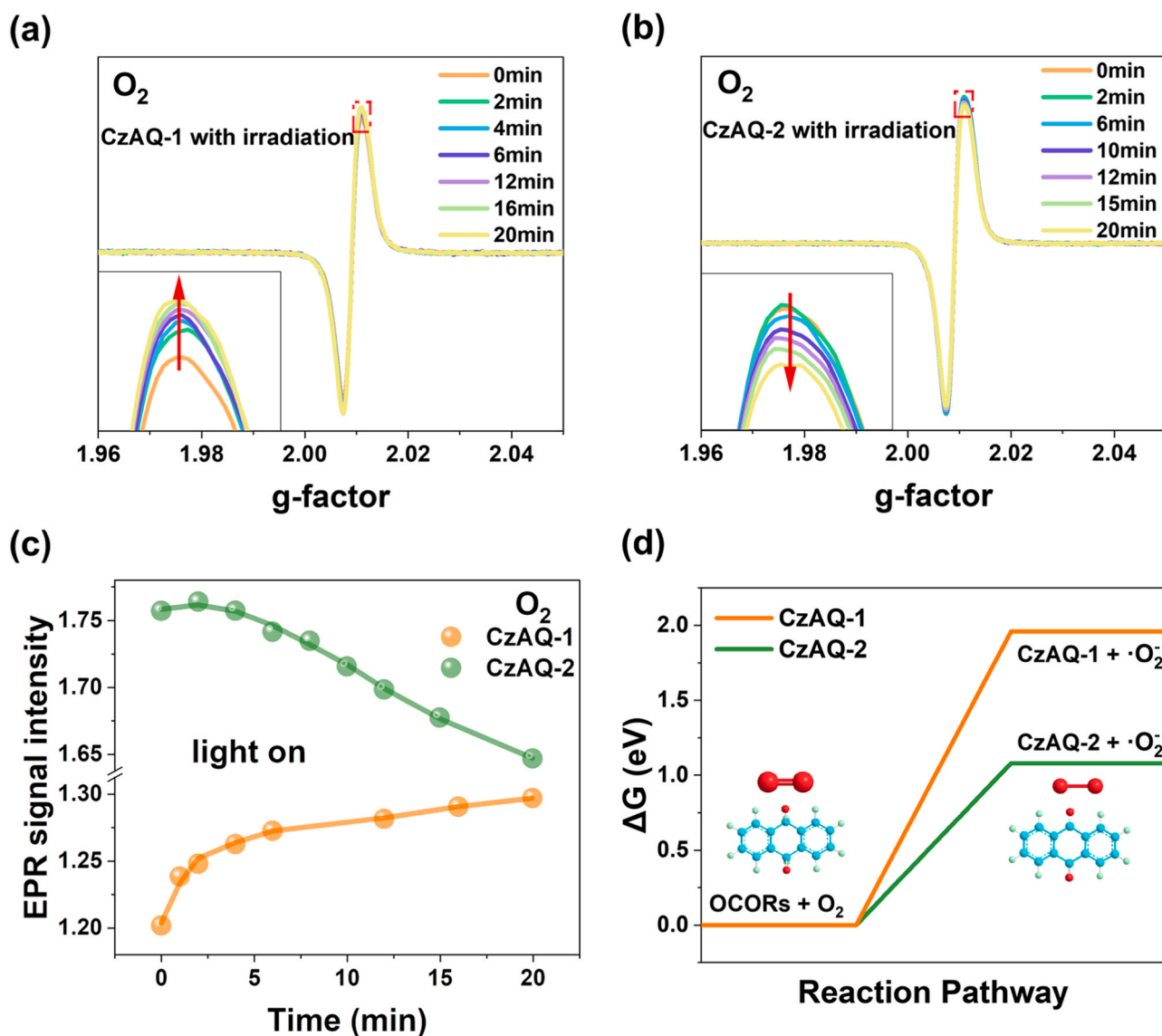


Fig. 8. The EPR spectra of (a) CZAQ-1 and (b) CZAQ-2 under oxygen atmosphere with light irradiation and (c) the corresponding signal intensities changes. (d) The Gibbs Free Energy (ΔG) of the reaction between OCORs in CZAQ-CPs and oxygen.

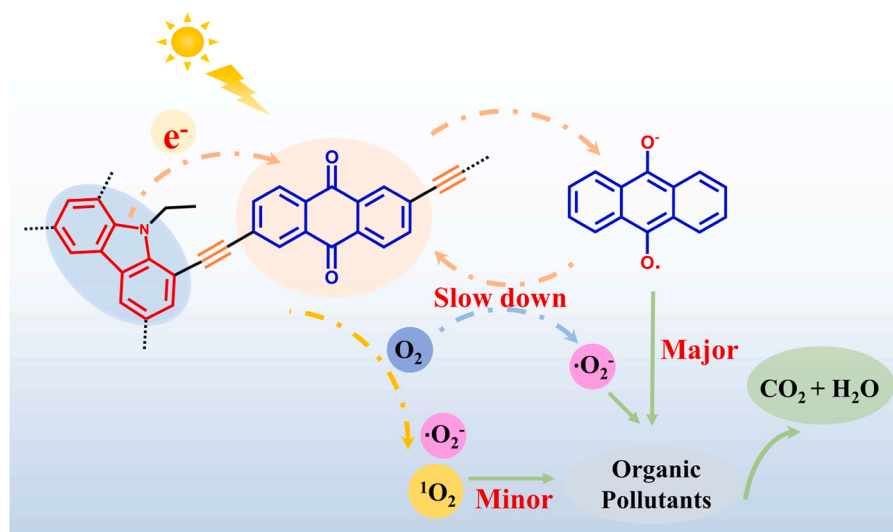


Fig. 9. Proposed mechanism for photocatalytic degradation of organic pollutants.

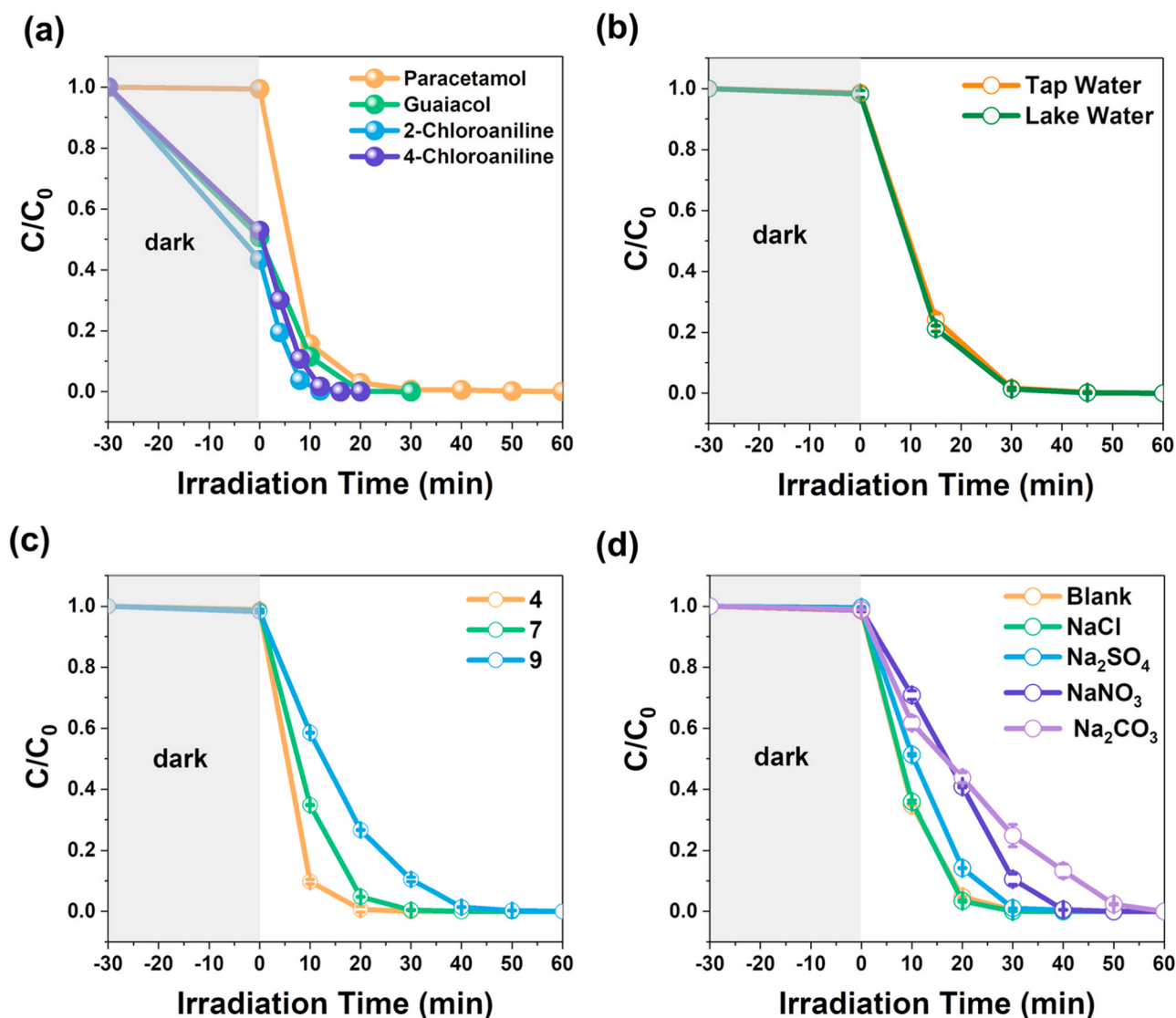


Fig. 10. (a) Photocatalytic degradation performance toward other four contaminants. Phenol degradation time profiles of CZAQ-1 (b) in different real water samples, (c) in different pH and (d) with different coexisting anions.

when the luminous intensity decreased from $100 \text{ mW} \cdot \text{cm}^{-2}$ to $10 \text{ mW} \cdot \text{cm}^{-2}$, the optical quantum density dropped significantly and the OCORs of CZAQ-2 reacted with oxygen at a faster rate than CZAQ-1, which resulted in a swift decline of OCORs in CZAQ-2 under low-intensity visible light. After the quenching of OCORs, the rapid reformation became challenging under low-intensity light conditions. Furthermore, the short lifetimes of $\cdot\text{O}_2$ prevented waiting for pollutant diffusion, leading to a significantly lower degradation performance of CZAQ-2 compared to CZAQ-1. Thus, it was supposed that OCORs of CZAQ-2 reacted more quickly with oxygen than CZAQ-1 to generate the $\cdot\text{O}_2$, which led to a comparatively worse degradation performance of CZAQ-2 than CZAQ-1 under low-intensity visible light.

3.7. Catalytic mechanism

The other two minor ROS $^1\text{O}_2$ and $\cdot\text{O}_2$ for photocatalytic degradation of phenol were further investigated and discussion in [Supporting Information Section 2.2](#). Both the signal of $^1\text{O}_2$ and $\cdot\text{O}_2$ radical were detected in all CZAQ-CPs by EPR experiment (Fig. S24). Furthermore, the capacity of $^1\text{O}_2$ and $\cdot\text{O}_2$ generation by CZAQ-CPs both followed the order of CZAQ-1 > CZAQ-2 > CZAQ-3 (Fig. S25 and S26). Therefore, a probable mechanism for efficient photocatalytic degradation (Fig. 9)

was proposed as follows: (1) CZAQ-1 was excited to generate the exciton under visible light irradiation and the singlet excited state was populated on the anthraquinone moiety. Then the exciton tended to separate into photo-induced electron and hole. (2) Electrons transferred from the carbazole-based group to the anthraquinone moiety, with each anthraquinone fragment storing one electron to form OCORs as the primary active species for degrading organic pollutants. Alternatively, charge transfer states can be formed and further transformed into triplet states by intersystem conversion. Charge transfer states can transfer electrons and energy to O_2 to generate $\cdot\text{O}_2$ and $^1\text{O}_2$ as minor active species. Ultimately, organic pollutants were effectively degraded by the three aforementioned highly reactive oxidative species.

3.8. Degradation performance in real water samples

In addition, the investigation extended to examining the photo-degradation universality of CZAQ-1 towards various organic pollutants in distillation water. Fig. 10a showed the photocatalytic degradation performance of CZAQ-1 on typical medicine and products, including paracetamol, Guaiacol, 2-chloroaniline and 4-chloroaniline. Notably, within a remarkably short span of 30 minutes, CZAQ-1 demonstrated the efficient degradation of these pollutants, indicating its potential for

outstanding photodegradation across diverse water contaminants. Furthermore, the photocatalytic degradation performance of CzaQ-1 was also assessed in actual water samples such as tap water (TW) and lake water (LW), with the specified parameters of TW and LW listed in Table S4. CzaQ-1 also maintained excellent photocatalytic performance towards phenol in both TW and LW (Fig. 10b). In addition, the mineralization rate of CzaQ-1, CzaQ-2 and CzaQ-3 were 44.3 %, 42.8 % and 54.1 %, respectively (Fig. S27). The comprehensive results underscored the practical application potential of CzaQ-1 in effectively degrading phenol and various contaminants, affirming its versatility and efficacy in water purification processes.

In practical water applications, the anti-interference capability was also the important factors to evaluate the performance of photocatalysts. CzaQ-1 exhibited excellent photocatalytic degradation performance toward phenol across a broad pH range from 4 to 9 (Fig. 10c). Furthermore, the presences of co-existing Cl^- , NO_3^- , SO_4^{2-} or CO_3^{2-} anions in solutions had negligible effect towards the degradation performance of phenol by CzaQ-1 (Fig. 10d).

4. Conclusion

In this study, we have successfully developed an efficient, stable, and highly interference-resistant carbazole-acetylene-anthraquinone photocatalyst. This catalyst can fully degrade various organic pollutants in just 30 minutes under $100 \text{ mW}\cdot\text{cm}^{-2}$ and 90 minutes under $10 \text{ mW}\cdot\text{cm}^{-2}$ visible light, while maintaining its performance over 10 cycles without significant deterioration. Furthermore, it exhibits outstanding performance in degrading organic pollutants in complex water matrices, such as tap water and lake water. Our systematic characterization has unequivocally confirmed that this catalyst primarily relies on OCORs as the main active species. The key to its exceptional performance lies in its ability to effectively mitigate the reaction between OCORs and oxygen, thereby preventing OCOR quenching. Importantly, in-depth research has revealed that CzaQ-1 strategically reduces the electrostatic potential of oxygen atoms in the anthraquinone moiety, further slowing down the OCORs-oxygen reaction. This results in an extended lifespan of OCORs in the air, allowing them to effectively wait for the diffusion of pollutants. Consequently, this catalyst is particularly suitable for practical water environments characterized by internal filtering effects and low pollutant concentrations. Moreover, we have also investigated the generation concentration and regulation of secondary active species, including singlet oxygen and superoxide radicals. This investigation has demonstrated the positive impact of efficient exciton dissociation during photophysical processes and electron transfer during the interfacial charge transfer process on the generation of these active species. In summary, this research provides novel strategies for controlling OCORs and lays the theoretical foundation for the practical application of photocatalysis in water treatment.

CRedit authorship contribution statement

Yingyi Cheng: Writing – original draft, Software, Methodology, Data curation. **Yu-Xin Ye:** Writing – review & editing, Supervision, Funding acquisition, Conceptualization. **Gangfeng Ouyang:** Funding acquisition. **Yuyan Huang:** Methodology, Data curation. **Huijie Yan:** Methodology, Data curation. **Liwei Zhang:** Methodology, Data curation. **Fang Zhu:** Funding acquisition.

Declaration of Competing Interest

The authors declare that they have no known competing financial interests or personal relationships that could have appeared to influence the work reported in this paper.

Data availability

Data will be made available on request.

Acknowledgements

This work was supported by the National Natural Science Foundation of China (Grant 22336007 and 22206209), and the Natural Science Foundation of Guangdong Province 2022A1515011953.

Appendix A. Supporting information

Supplementary data associated with this article can be found in the online version at doi:10.1016/j.apcatb.2024.124166.

References

- [1] R. Pashaei, R. Dzingeleivičienė, A. Bradauskaitė, et al., Pharmaceutical and microplastic pollution before and during the COVID-19 pandemic in surface water, wastewater, and groundwater, *Water* 14 (19) (2022) 3082.
- [2] M.B. Andrade, T.R.T. Santos, A.C.S. Guerra, et al., Evaluation of magnetic nano adsorbent produced from graphene oxide with iron and cobalt nanoparticles for caffeine removal from aqueous medium, *Chem. Eng. Process* 170 (2022) 108694.
- [3] E.F.D. Januário, Y.J. Fachina, G. Wernke, et al., Application of activated carbon functionalized with graphene oxide for efficient removal of COVID-19 treatment-related pharmaceuticals from water, *Chemosphere* 289 (2022) 133213.
- [4] Z. Chen, F. Anand, Y. Zhang, et al., Single-atom Mo–Co catalyst with low biotoxicity for sustainable degradation of high-ionization-potential organic pollutants, *Proc. Natl. Acad. Sci.* 120 (29) (2023).
- [5] M. Li, D. Liand, Z. Zhou, et al., Plasmonic Ag as electron-transfer mediators in $\text{Bi}_2\text{MoO}_6/\text{Ag}-\text{AgCl}$ for efficient photocatalytic inactivation of bacteria, *Chem. Eng. J.* 382 (2020) 122762.
- [6] Q. Wang, X. Fang, P. Hao, et al., Green preparation of porous hierarchical TiO_2 (B)/anatase phase junction for effective photocatalytic degradation of antibiotics, *Chem. Commun.* 57 (96) (2021) 13024–13027.
- [7] Q. Wang, X. Wang, P. Hao, et al., Facile green synthesis of a dahlia-like anatase/ TiO_2 (B) phase junction for boosting the photocatalytic degradation of persistent tetracycline, *Catal. Sci. Technol.* 13 (1) (2023) 56–61.
- [8] J.Y. Yue, L.P. Song, Y.F. Fan, et al., Thiophene-containing covalent organic frameworks for overall photocatalytic H_2O_2 synthesis in water and seawater, *Angew. Chem. Int. Ed.* 62 (38) (2023).
- [9] C. Chu, D. Yao, Z. Chen, et al., Cyano-regulated organic polymers for highly efficient photocatalytic H_2O_2 production in various actual water bodies, *Small* 19 (46) (2023).
- [10] P. Liu, L. Xing, H. Lin, et al., Construction of porous covalent organic polymer as photocatalysts for RhB degradation under visible light, *SCI BULL* 62 (13) (2017) 931–937.
- [11] Y. Ye, J. Pan, Y. Shen, et al., A solar-to-chemical conversion efficiency up to 0.26 % achieved in ambient conditions, *Proc. Natl. Acad. Sci. USA* 118 (46) (2021).
- [12] H. Yan, M. Shen, Y. Shen, et al., Spontaneous exciton dissociation in organic photocatalyst under ambient conditions for highly efficient synthesis of hydrogen peroxide, *Proc. Natl. Acad. Sci.* 119 (22) (2022).
- [13] W. Zou, Y. Cheng, Y.X. Ye, et al., Metal-free Photocatalytic CO_2 reduction to CH_4 and H_2O_2 under Non-sacrificial Ambient Conditions, *Angew. Chem. Int. Ed.* 62 (49) (2023).
- [14] Y. Ye, C. Wen, J. Pan, et al., Visible-light driven efficient overall H_2O_2 production on modified graphitic carbon nitride under ambient conditions, *Appl. Catal. B* 285 (2021) 119726.
- [15] X. Wang, Y. Cheng, Y. Yuan, Y. Zhang, W. Wang, Structures and electron affinity energies of polycyclic quinones, *Heliyon* 8 (8) (2022) e10107.
- [16] H. Korthand, P. Mulder, Phenolic hydrogen transfer by molecular oxygen and hydroperoxyl radicals. insights into the mechanism of the anthraquinone process, *J. Org. Chem.* 85 (4) (2020) 2560–2574.
- [17] E.M. Rodríguez, U. von Gunten, Generation of hydroxyl radical during chlorination of hydroxyphenols and natural organic matter extracts, *Water Res* 177 (2020) 115691.
- [18] Y.Z. Peng, G.C. Guo, S. Guo, et al., Charge transfer from donor to acceptor in conjugated microporous polymer for enhanced photosensitization, *Angew. Chem. Int. Ed.* 133 (40) (2021) 22233–22240.
- [19] L. Chen, L. Wang, Y. Wan, et al., Acetylene and diacetylene functionalized covalent triazine frameworks as metal-free photocatalysts for hydrogen peroxide production: a new two-electron water oxidation pathway, *Adv. Mater.* 32 (2) (2020).
- [20] W. Zhao, P. Yan, B. Li, et al., Accelerated synthesis and discovery of covalent organic framework photocatalysts for hydrogen peroxide production, *J. Am. Chem. Soc.* 144 (22) (2022) 9902–9909.
- [21] L. Liu, M. Gao, H. Yang, et al., Linear conjugated polymers for solar-driven hydrogen peroxide production: the importance of catalyst stability, *J. Am. Chem. Soc.* 143 (46) (2021) 19287–19293.

- [22] H. Yan, Y. Dengand, M. Shen, et al., Regulation the reactive oxygen species on conjugated polymers for highly efficient photocatalysis, *Appl. Catal. B* 314 (2022) 121488.
- [23] Y. Hou, F. Liu, B. Zhangand, M. Tong, Thiadiazole-based covalent organic frameworks with a donor-acceptor structure: modulating intermolecular charge transfer for efficient photocatalytic degradation of typical emerging contaminants. *Environ. Sci. Technol.* 56 (22) (2022) 16303–16314.
- [24] H. Yan, Y. Pengand, Y. Huang, et al., Enhancing photosynthesis efficiency of hydrogen peroxide by modulating side chains to facilitate water oxidation at low-energy barrier sites, *Adv. Mater.* (2024).
- [25] M. Nakano, Open-shell-character-based molecular design principles: applications to nonlinear optics and singlet fission, *Chem. Rec.* 17 (1) (2017) 27–62.
- [26] B. Liu, J. Liand, D. Liu, et al., Electron-withdrawing bulky group substituted carbazoles for blue TADF emitters: simultaneous improvement of blue color purity and RISC rate constants, *Dyes Pigments* 203 (2022) 110329.
- [27] S.C. Núñez Montoya, L.R. Cominiand, M. Sarmiento, et al., Natural anthraquinones probed as Type I and Type II photosensitizers: singlet oxygen and superoxide anion production, *J. Photochem. Photobiol. B, Biol.* 78 (1) (2005) 77–83.
- [28] H. Sun, Z. Langand, Y. Zhao, et al., Copper-Bridged Tetrakis(4-ethynylphenyl) ethene Aggregates with Photo-Regulated $^1\text{O}_2$ and O_2^- Generation for Selective Photocatalytic Aerobic Oxidation, *Angew. Chem. Int. Ed.* 61 (29) (2022).
- [29] J. Chen, Y. Wang, F. Wangand, Y. Li, Photo-Induced Switching of CO_2 Hydrogenation Pathway towards CH_3OH Production over $\text{Pt@UiO-66-NH}_2(\text{Co})$, *Angew. Chem. Int. Ed.* (2023).
- [30] J. Dou, Y. Tangand, Z. Lu, et al., Neglected but efficient electron utilization driven by biochar- coactivated phenols and peroxydisulfate: polyphenol accumulation rather than mineralization, *Environ. Sci. Technol.* 57 (14) (2023) 5703–5713.
- [31] Y. Fu, Y. Qianand, A. Zhang, et al., Long-acting ultraviolet-blocking mechanism of lignin: generation and transformation of semiquinone radicals, *ACS Sustain. Chem. Eng.* 10 (17) (2022) 5421–5429.
- [32] N. Li, G. Laiand, L. Chung, et al., Achieving high CO_2 photoreduction activity by conductive crosslinks of metal-organic framework, *CCS Chem.* (2023) 1–11.
- [33] Z. Lan, M. Wuand, Z. Fang, et al., A fully coplanar donor - acceptor polymeric semiconductor with promoted charge separation kinetics for photochemistry, *Angew. Chem. Int. Ed.* 60 (30) (2021) 16355–16359.
- [34] M. Sachs, R.S. Sprickand, D. Pearce, et al., Understanding structure-activity relationships in linear polymer photocatalysts for hydrogen evolution, *Nat. Commun.* 9 (1) (2018).
- [35] Z. Fu, C. Shuand, X. Wang, et al., Fluorinated covalent organic frameworks coupled with molecular cobalt cocatalysts for efficient photocatalytic CO_2 reduction, *CCS Chem.* 5 (10) (2023) 2290–2300.
- [36] Z. Liu, T. Luand, Q. Chen, An sp-hybridized all-carboatomic ring, cyclo[18]carbon: electronic structure, electronic spectrum, and optical nonlinearity, *Carbon* 165 (2020) 461–467.
- [37] Y. Qian, Y. Hanand, X. Zhang, et al., Computation-based regulation of excitonic effects in donor-acceptor covalent organic frameworks for enhanced photocatalysis, *Nat. Commun.* 14 (1) (2023).
- [38] Y. Abiko, Y. Nakaiand, N.C. Luong, et al., Interaction of quinone-related electron acceptors with hydropersulfide Na_2S_2 : evidence for one-electron reduction reaction, *Chem. Res. Toxicol.* 32 (4) (2019) 551–556.
- [39] Z. Wang, R. Jiaand, Y. Chen, et al., Supramolecular semiquinone radicals confined with DNazymes for dissipative ROS generation and therapy, *Nano Today* 43 (2022) 101402.
- [40] E.A. Bisong, H. Louisand, T.O. Unimuke, et al., Vibrational, electronic, spectroscopic properties, and NBO analysis of p-xylene, 3,6-difluoro-p-xylene, 3,6-dichloro-p-xylene and 3,6-dibromo-p-xylene: DFT study. *HELIYON* 6 (12) (2020).
- [41] T. Luand, F. Chen, Multiwfn: a multifunctional wavefunction analyzer, *J. Comput. Chem.* 33 (5) (2012) 580–592.
- [42] H. Che, J. Wangand, P. Wang, et al., Simultaneously achieving fast intramolecular charge transfer and mass transport in Holey D- π -a organic conjugated polymers for highly efficient photocatalytic pollutant degradation, *JACS Au* 3 (5) (2023) 1424–1434.